Carbon 136 (2018) 255–261

Contents lists available at ScienceDirect

Carbon

journal homepage: www.elsevier.com/locate/carbon

Surface structure of few layer graphene

Liangzhi Zhou [a], Laura Fox [a, b], Magdalena Włodek [c], Luisa Islas [a], Anna Slastanova [a], Eric Robles [d], Oier Bikondoa [e, f], Robert Harniman [a], Neil Fox [a], Mattia Cattelan [a], Wuge H. Briscoe [a, *]

[a] School of Chemistry, University of Bristol, Cantock's Close, Bristol, BS8 1TS, UK
[b] Bristol Centre for Functional Nanomaterials, HH Wills Laboratory, University of Bristol, Tyndall Avenue, BS8 1TL, UK
[c] Jerzy Haber Institute of Catalysis and Surface Chemistry, Polish Academy of Sciences, Niezapominajek 8, Poland
[d] Household Care Analytical, Procter & Gamble Newcastle Innovation Centre Whitley Road, Longbenton, Newcastle, NE12 9TS, UK
[e] XMaS, The UK-CRG, European Synchrotron Radiation Facility (ESRF), 6 Rue Jules Horowitz, BP 220, 38043, Grenoble CEDEX 9, France
[f] Department of Physics, University of Warwick, Gibbet Hill Road, Coventry, CV4 7AL, UK

ARTICLE INFO

Article history:
Received 17 December 2017
Received in revised form
22 April 2018
Accepted 29 April 2018
Available online 2 May 2018

ABSTRACT

Understanding surface structure of graphene is important for its integration into composite materials. Here, we have used synchrotron X-ray reflectivity (XRR) to study the structure of commercially available graphene samples (prepared *via* chemical vapor deposition, and marketed as *graphene monolayers*) on SiO_2/Si at different temperatures. X-ray photoelectron spectroscopy, photoemission electron microscopy and atomic force microscopy (AFM) were employed to evaluate the composition and morphology of the graphene layer. Our results indicate that the samples we characterized consisted of 3–4 layers of graphene, which should thus be more accurately described as *few layer graphene* (FLG). Furthermore, a "contaminant" layer, comprising polymethylmethacrylate and graphene multilayers, was found present atop FLG. We also report tentative results on the effect of temperature on the graphene sample thickness. At 25 °C, the FLG thickness from XRR measurements was 13.0 ± 1.0 Å, in agreement with that obtained from AFM (13.9 ± 0.7 Å). Upon heating to 60 °C, the FLG thickness expanded to 13.8 Å, which further increased to 14.3 Å upon cooling to 25 °C. We attribute this temperature dependent thickness to the out-of-plane rippling of graphene as previously reported. These unprecedented results on the FLG surface structure are valuable to its potential bioanalytical applications.

1. Introduction

Graphene is a one-atom thick, flat, carbon monolayer with a hexagonal carbon aromatic structure. As one of the basic carbon allotropes, it can be transformed into other carbon materials, such as carbon nanotubes and fullerenes. Since the 1970s, studies on growing graphene monolayers on crystals have been carried out, and the first graphene was successfully exfoliated in 2004 by Novoselov and Geim [1]. The unique 2D electronic properties of graphene have since stimulated numerous studies aiming to develop its use in applications such as supercapacitors, batteries, interconnects, transistors, phonon detectors, and sensors *etc.*[2]. Concurrently, advances in the production and modification of graphene sheets have continued to stimulate interest in its potential application in biotechnology [3]. For instance, the surface charging of graphene due to ion adsorption has been exploited to monitor pH changes [4] and lipid membrane disruptions [5].

One of the most promising methods for producing high quality graphene on an industrial scale is chemical vapor deposition (CVD), which involves depositing graphitic layers atop another crystalline substrate, such as SiC [6], Ni [7], and Cu [8]. A polymethylmethacrylate (PMMA) coating is deposited atop *via* spin coating, and then the graphene can be transferred onto a desired substrate (*e.g.* SiO_2) after the original substrate is removed by chemical etching [9–12]. Graphene prepared by the CVD method has been reported to exhibit an electronic spectrum that can be described by a 2D analogue of the Dirac equation, similar to that of free-standing graphene [3]. Among all the substrates, Cu attracted particular attention. As confirmed by Raman spectroscopy, graphene deposited on Cu by the CVD method could yield over 93%

* Corresponding author.
E-mail address: wuge.briscoe@bristol.ac.uk (W.H. Briscoe).

https://doi.org/10.1016/j.carbon.2018.04.089

coverage (with the rest consisting of 2–3 layer graphene), thanks to its weak interaction with graphene which benefits 2D crystal growth, thereby generating monolayer graphene on the Cu surface [13]. However, it is known that one of the issues with the transferred CVD graphene is the residues of PMMA and etching agents [9–12].

Previous studies have shown that the physical properties of graphene materials are determined by their structure, specifically the thickness and the defects or contaminants. For example, the thermal conductivity of graphene materials increases with the layer number, with monolayer, double-layer, and *few layer graphene* (FLG) (3–10 layers) showing different 2D electronic properties [14,15]; the transport properties in epitaxial graphene are influenced by its sp^2 aromatic lattice structure, which is in turn affected by its substrate and growth conditions [16,17]; and the presence of ripples and wrinkles on graphene is expected to have a negative effect on its electronic properties [13]. Thus, a precise determination of the thickness and morphology of graphene samples under different conditions is important.

Different techniques have been employed for the structural characterisation of graphene and its derivatives, as listed and compared in Table S1 in the Supporting Information (SI). For instance, graphene on silica was first revealed by optical microscopy, scanning electron microscopy (SEM), and atomic force microscopy (AFM) [1]. Non-destructive techniques such as electron microscopy (EM), Raman/Rayleigh scattering microscopy [10], ellipsometry [11,12], and near edge X-ray absorption spectroscopy (NEXAS) [18,19] have been used to study the graphene structure and/or its adsorbates. For the in-plane structural characterisation, scanning tunnelling microscopy (STM) and scanning tunnelling spectroscopy (STS) [8,13,16,25] have been used to image the graphene lattice. X-ray photoelectron spectroscopy (XPS) and Auger electron spectroscopy (AES) [6,26,27] assisted by low energy electron microscopy (LEEM) and photoemission electron microscopy (PEEM) measurements [17,25,28–30] have also been employed for the compositional, structural and morphological characterisation of graphene on conductive substrates. AFM [20], total internal reflection fluorescence correlation spectroscopy (ITIR-FCS) [5], and quartz crystal microbalance with dissipation monitoring (QCM-D) [20] have been used to study lipid adsorption on graphene and related systems. However, these techniques have a limited capacity to probe the out-of-plane structure of the adsorbed layer.

Another powerful technique is X-ray reflectivity (XRR), which is widely used for probing buried interfaces and thin film monolayers [21], bilayers [22,23] and multilayers [24] structures. XRR has been used to study the structure of graphene coated with other popular materials in electronic devices (*e.g.* HfO_2 [25], Au [26], and perylenetetracarboxylic dianhydride (PTCDA) [27]), and exposed and buried interfacial structures of graphene grown on SiC [28,29], showing its potential to be used on the structural characterization of graphene.

In this study, commercially available graphene samples on Si/SiO_2 widely used in the studies of graphene applications have been studied using synchrotron XRR. XPS, PEEM and AFM were also used to provide complementary information on the composition and morphology of the samples. Our findings are valuable to graphene research and applications, and also demonstrat the suitability of XRR as a sensitive method for characterising the graphene surface structure, paving the way for further investigations of biomolecular structures on graphene using XRR.[1]

2. Experimental methods

2.1. Materials

Graphene samples prepared by an established CVD method were purchased from *Graphenea Inc*.[2] Briefly, the preparation process involves chemical vapor deposition of methane on a copper (Cu) foil to produce a graphene (mono)layer. Then a PMMA coating is deposited atop *via* spin coating, before the copper foil is etched away. Finally, the graphene is transferred onto a 1 cm × 1 cm Si wafer with a 300 nm SiO_2 top layer. Graphene produced is being marketed as "*monolayer graphene*", and is widely used in the studies to evaluate potential application of graphene monolayers in electronic devices.

2.2. Experiment methods

The AFM investigation was conducted in ambient conditions using a MultiMode VIII microscope with a NanoScope V controller, utilizing PeakForce feedback control (Bruker, CA, USA). The cantilever employed was SCANASYST_FLUID+ with nominal spring constant and tip radius of 0.7 N m^{-1} and 2 nm respectively.

XPS and PEEM measurements of the graphene samples were performed at the Bristol NanoESCA facility. XPS measurements of the FLG were performed with an Argus spectrometer before and after annealing at 450 °C at an ultra-high vacuum (UHV) base pressure of 4.0×10^{-11} mbar for 1 h. Core-level photoemission spectra were acquired at 45° w.r.t. the sample surface, using a monochromatic Al Kα (1486.7 eV) X-ray source with a pass energy of 20 eV at room temperature and an estimate total energy resolution of 600 meV. The relative composition of C, O, and Si can be calculated from their corresponding photoemission line intensities.

The PEEM was performed using a NanoESCA II, and the measurements were carried out at room temperature under the UHV condition with a pass energy of 50 eV, a lateral resolution of 150 nm, and an overall energy resolution of 140 meV. The energy calibration was confirmed by fitting a Fermi edge of a clean metallic substrate at the same measurement condition. A He I (21.2 eV) discharge lamp was used as excitation source, and the absolute work function measurement for a particular sample area was obtained from electronic counting of the emitted photoelectrons [30]. The work function values in the maps were obtained by fitting the 600 × 600 camera pixels spectra with an "error function". The low excitation photon energy makes PEEM extremely surface sensitive (to 2–3 atomic surface layers), and the PEEM images were acquired after cleaning by annealing to show the surface morphology.

Synchrotron XRR measurements were performed at beamline BM28-XMaS, European Synchrotron Radiation Facility (ESRF), Grenoble, France. A custom designed sample cell was used in all XRR experiments, as shown schematically in Fig. 1 [23,31]. The cell, originally designed to accommodate the "bending mica method" [21], consists of a chamber to house the sample stage for both curved and flat substrates. Temperature control in the range 10–90 °C is facilitated by two brass jackets sandwiching the chamber, one to house electrical heaters and the other connected to a water bath to provide cooling. Graphene samples were mounted on the sample stage in the XRR cell, which was sealed *via* two polyester (Mylar®) windows.

The X-ray beam energy was 14 keV (wavelength $\lambda = 0.8856$ Å), and the incident beam size defined by aperture slits was 100 μm (vertical FWHM) × 255 μm (horizontal FWHM). XRR scans were

[1] L. Zhou et al., "Evidence for air bubble formation on graphene surface in water", in preparation.

[2] https://eu.graphenea.com/.

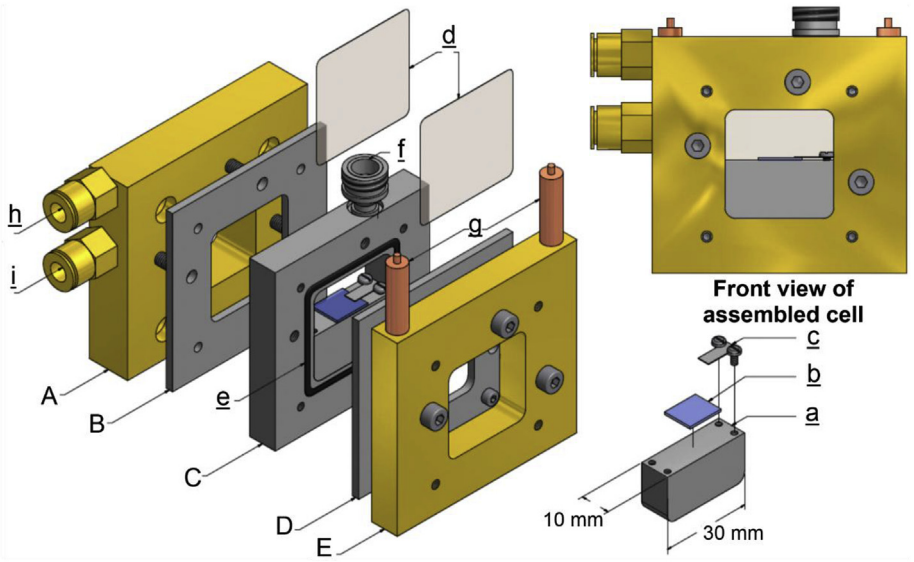

Fig. 1. Key components of the XRR cell, consisting of three stainless steel plates (B–D), and the cooling (A) and heating jackets (E). Two Mylar® windows (d) are clamped between plates B, D and plate C, creating a liquid chamber with a capacity of 5 ml. Sealing is facilitated by means of O-rings placed in grooves (e). The samples (b) 1 cm × 1 cm in size are clamped by two small plates (c), onto a stainless steel stage (a). A nozzle (f) allows *in situ* liquid/gas exchange. The heating jacket can be controlled by two heaters (g) while the cooling jacket can be connected to a water circulating bath *via* an inlet (i) and an outlet (h). (A colour version of this figure can be viewed online.)

collected at 25 °C, 40 °C and 60 °C in air, with the incident angle θ_i varying from 0.06 to 3.0°, corresponding to a $\boldsymbol{Q}$ range of 0.015–0.74 $Å^{-1}$, where the vertical momentum transfer vector $\boldsymbol{Q} = 4\pi\sin\theta/\lambda$. The specular reflections were detected at each angle ($\theta_r = \theta_i$) using an Avalanche Photodiode Detector (APD). XRR data fitting was performed by using *Motofit* in *Igor Pro* (WaveMetrics, Inc., Lake Oswego, OR, USA) [32]. For reflectivity data collected on a well-defined flat substrate such as silicon, the surface layer was modelled as stacked homogeneous slabs. Each layer can be described by three parameters: the scattering length density (SLD, ρ), thickness t, and inter-slab roughness R_a. These parameters were varied in the total reflectivity calculation using the Abeles matrix method, and a genetic algorithm optimisation was adopted to obtain the best fitting for the curves. This generates the same result as Parratt's Recursive method [32]. The analysis of XRR results is described in the Supporting Information (SI) section SI-2.

Ellipsometry was performed using a J.A. Wollam M-2000 ellipsometer (J.A. Woollam Company, Incorporated, Lincoln, NE, USA), to obtain the total thickness of the graphene sample, using a white light source (wavelengths of 245–1000 nm) at a fixed incident angle of 75°. The obtained data was processed and fitted using VASE 32 software from J.A. Wollam adopting a three-layer model (consisting of a silicon substrate, a silicon dioxide layer and a graphene layer). The static contact angle of a water droplet on the graphene sample was 76.77°±0.53° as measured using the Sessile drop method on KRÜSS® DSA100 (see SI-5).

It is useful to compare the footprint size of different complementary methods when interpreting the results. For XPS it was approximately an oval with major/minor axes of 3mm/2 mm; for PEEM it was 60 μm × 60 μm; for XRR it was 255 μm × 1 cm (the projection of the vertical beam size onto the sample); for ellipsometry the circular spot size was ~3 mm in diameter; for AFM, the scan size was either 5 μm × 5 μm or 1 μm × 1 μm; and for the contact angle measurement, the diameter of the water droplet was of ~3.3 mm. As such, AFM and PEEM provided localised morphological and chemical information, whilst XRR, XPS, ellipsometry, and contact angle provided average structural information across a larger sample area. It is also worth bearing in mind the different conditions for these measurements: XPS and PEEM were carried out under UHV (3×10^{-11} mbar), whilst the rest of the measurements were performed under ambient conditions.

3. Results and discussion

The XPS spectra from the survey scans of a wide bonding energy range on the FLG sample before and after annealing in UHV at 450 °C are shown in Fig. 2a. In both cases, only the presence of C, O, and Si was observed, and no metal residues from the original copper substrate and the etchant were observed on the sample. The elemental compositions estimated from the spectra show that, before annealing, the atomic composition of C, O, and Si was 32.2%, 36.7% and 31.1%, respectively; and after annealing, the percentage of C decreased to 17.4%, but those of O and Si increased to 42.6% and 40.0%, respectively. The C 1s photoemission lines before and after annealing in Fig. 2b show clear differences in their shape and relative intensity. Deconvolution of these photoemission lines (Fig. 2c and d; Table S4) indicates the presence of C 1s (sp^2 and sp^3), C-OH and O-C=O [33–35] before annealing, whereas after annealing, the intensity of the C-OH and C=O peaks dropped remarkedly.

The CVD method is known to produce graphene with an ordered structure and exceptional electronic properties. However, the substrates on which graphene can be grown are limited, and typically transition metals are used. Subsequently, epitaxial graphene often needs to be transferred from the original growth substrate, a process that could cause contamination [9,10,12]. In this case, there were four possible types of contaminants: the multilayer graphene formed on top of the single layer graphene, the PMMA used for transferring, residues due to incomplete Cu dissolution [11,36], and etchant liquid residues (typically $FeCl_3$). We ascribe the observed changes in the XPS carbon peaks in Fig. 2 to PMMA residues being removed by the annealing procedure. This explanation is consistent with the observed decreased C composition (from 32.2% to 17.4%) and C/Si ratio (from 1.03 to 0.44) after annealing. Note that the XPS detection limit was ~0.1 atomic% in our measurements.

The annealed samples were further investigated by PEEM, an extremely surface sensitive technique, to reveal their surface morphology, which also helps to identify any possible

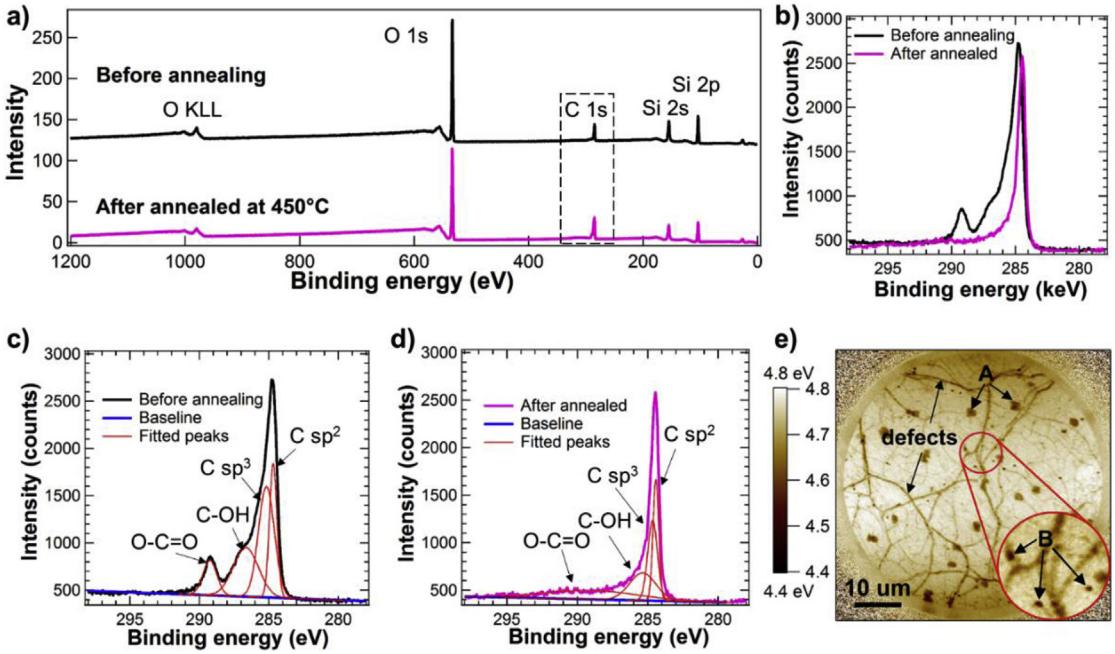

Fig. 2. a) The XPS surveys for the graphene sample measured before (black line) and after (pink line) annealing. b) shows the C 1s photoemission region highlighted in the dashed rectangle in a), and the fittings for the photoemission lines before and after annealing are shown in c) and d), respectively. The fittings suggest the existence of carbon oxides in the sample, including O-C=O and C-OH, with the peak energy values listed in Table S4 in SI-3. After annealing, the amount of the oxides decreased. e) The work function map of graphene annealed at 450 °C for 1 h, with 2 types of contaminants labelled as **A** and **B**. (A colour version of this figure can be viewed online.)

contaminants on the graphene surface due to the contrast in their work function. Work function is the energy needed to excite an electron from the Fermi level of the material to free space. An example work function map in Fig. 2e shows darkened (lower work function) lines and spots appearing on a continuous light background (higher work function). We attribute the dark lines to defects (cracks) likely caused by the transferring process [9], and the spots to two types of contaminants (examples labelled as **A** and **B** on Fig. 2e). Contaminants **A** (of size ~2 μm) were found sparsely over the sample surface, while **B** (of size ~500 nm) were found in the vicinity of the defects. The work function of annealed graphene (*i.e.* the light background in Fig. 2e) was ~4.7–4.8 eV, which is slightly larger than the reported work function of intrinsic graphene (4.56 eV) [37]. This difference could be related to the redistribution of electrons between the substrate and graphene [7,38,39]. Upon annealing, the defects and contaminants **A** remained, whereas contaminants **B** with a lower work function of ~4.3–4.6 eV gradually disappeared. We thus attribute **B** to PMMA residues from the transferring process of the graphene from its Cu substrate during fabrication. These PMMA residues were removed upon annealing at 450 °C, an interpretation consistent with a previous study which showed that PMMA was burnt off from the graphene surface at high temperatures in UHV [11,36].

The formation of multilayer graphene with a size of few micrometres on monolayer graphene grown on Cu has been previously characterised by Raman spectroscopy [8]. FLG with more than 3 graphene monolayers exhibited a work function of 4.6 eV, similar to that of graphite [7,40,41]. Thus, contaminants **A** with a work function of ~4.6 eV were likely graphene multilayers.

Fig. 3a shows a topographic AFM image on a1 μm × 1 μm scale, and three line profiles along the coloured lines (with arrows pointing towards the directions of the profiles taken) are shown in Fig. 3b shown in the corresponding colours. By analysing the topological histograms of the AFM images, the position and the thickness of the FLG layer can be obtained, as described in SI-4. The highlighted areas in the line profiles represent the position of the graphene layer from the histogram analysis, and the PMMA residues with thickness in the range of 0–57 Å were seen on top of the graphene surface. Fig. 3c shows an AFM topological image over a larger scale (5 μm × 5 μm), indicating the deposited graphene appeared continuous with a number of defects (dark holes, *i.e.* **1** in Fig. 3c) of size ~100 nm and a small number of PMMA residues appearing as elevated (lighter) spots. The PMMA residues varied in size (~10–100 nm), and two such spots (**2 and 3**) are circled in the figure. The red rectangle **(4)** in Fig. 3c highlights a crack defect on the graphene surface with PMMA partially filling the crack. This interpretation agrees with the work function map (Fig. 2e), where PMMA was detected around the defects. The apparent thickness of the graphene layer from the height histogram on a scale described in SI-4 is 13.9 ± 0.7 Å, which includes any (small) spacing between graphene and the underlying SiO_2 substrate. The graphene layer thickness points to the presence of the FLG instead of a graphene monolayer, in agreement with numerous AFM studies determining the thickness of graphene and FLG on flat substrates, with the reported thickness ranging from 3.5 Å to 15 Å, depending on the fabrication method and the AFM imaging [1,42–44].

Assuming PMMA residues existed mostly atop the measured sample, from the height histogram analysis, the graphene coverage on SiO_2 was ϕ_g 85.1 ± 2.1%, as described in SI-4. However, if the graphene did not remain intact during the transferring process, PMMA could have been transferred onto silica instead of graphene; in that case, the graphene coverage would have been overestimated, whilst that of PMMA underestimated.

The XRR curves of the graphene samples are shown in Fig. 4b. These curves were collected at 25 °C, 40 °C and 60 °C, and after the sample was cooled back down to 25 °C after heating. It is interesting to study such a temperature effect, given its relevance to potential biomedical applications of graphene. These results are representative from two separate synchrotron experiments on two different batches of samples from the same supplier. The open

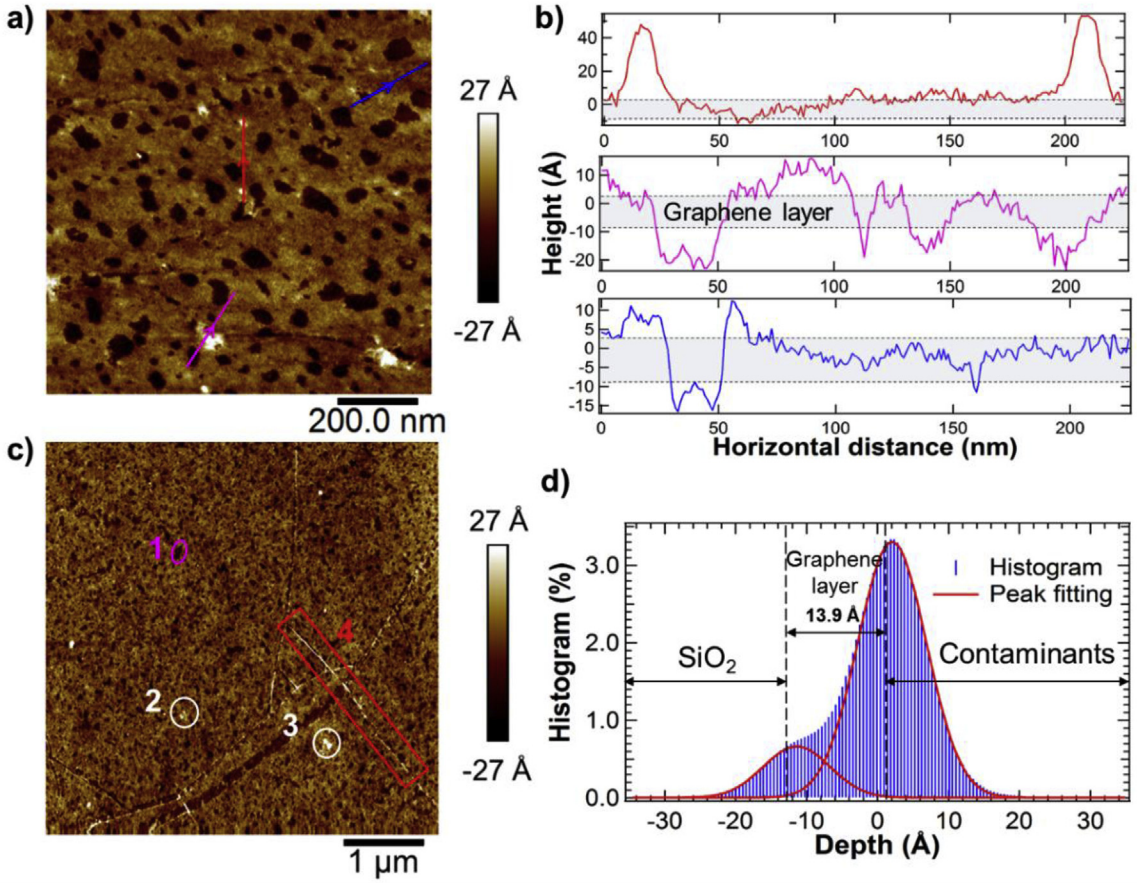

Fig. 3. a) An example AFM scale topological image on a 1 μm × 1 μm scale; b) Three line profiles followed the direction of the coloured arrow lines in a), with the grey highlighted areas attributed to the graphene layer; c) An example AFM topographic image on a 5 μm × 5 μm scale, highlighting PMMA residues (*e.g.* **2**, **3**) on a continuous graphene layer with holes (*e.g.* **1**) and defects (*e.g.* **4**) exposing underlying SiO_2; d) the corresponding histogram shows the height distribution of SiO_2, graphene, and the contaminant layer. (A colour version of this figure can be viewed online.)

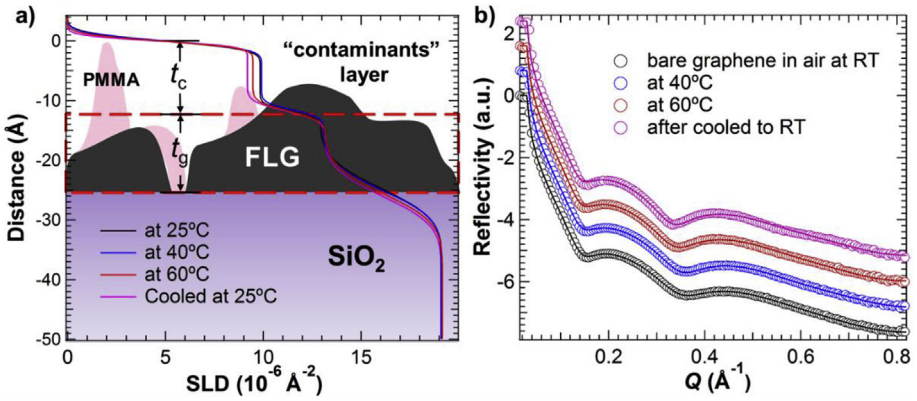

Fig. 4. a) The fitted SLD profile of the graphene sample at different temperatures with the corresponding physical model used for the fitting. Here, t_c and t_g are the thickness of the 2 slabs representing the contaminants and graphene, respectively. b) The open circles and solid lines are corresponded to the collected XRR data points and fits on a log scale of graphene plotted against **Q** at different temperatures (with the curves offset vertically for clarity). The fitting parameters are listed in Table 1. (A colour version of this figure can be viewed online.)

circles are the experimental data points, and the solid red lines the fits using a three-layer model, with the details of XRR analysis given in SI-2. The morphology and thickness measurement of graphene from AFM imaging (*cf.* Fig. 3) indicates that the graphene sample was not a graphene monolayer, but more likely FLG. PEEM (*cf.* Fig. 2) suggests that a "contaminant" layer was present atop the graphene layer, which was likely a mixture of graphene multilayers and PMMA residues. Therefore, when analysing the XRR data, we have used a three layer model (Fig. 4a): a contaminant layer (of thickness t_c) atop a graphene layer (t_g) attached to the substrate with a SiO_2 layer (t_s). The fitted thickness (t), inter-layer roughness (R_a) and SLD (ρ) are listed in Table 1. Overall, the structural information from fitting the XRR data is consistent with the observations from AFM and PEEM measurements.

Table 1
Fitting parameters for XRR results of graphene in air at different temperatures, using the three-layer model (*cf.* Fig. 4a). The SLD (ρ) of graphene and SiO_2 were fixed during fitting, and that of the contaminant layer was fitted in the range between air to graphene, since it is presumed a layer of a mixture with limited coverage instead of a homogeneous film. Also listed are the two fitted interfacial roughness values, $R_{a,c}$ for the roughness at the interface between air and the "contaminant" layer (thus the subscript c) and $R_{a,g}$ for that at the interface between the "contaminant" layer and the graphene layer.

T (°C)	t_g (Å)	$R_{a,g}$ (Å)	ρ (10^{-6} Å^{-2})	ϕ_g (%)	t_c (Å)	$R_{a,c}$ (Å)	ρ (10^{-6} Å^{-2})	χ^2 (10^{-3})
25	12.9	0.9	12.91	70.9	11.8	1.2	9.80	1.21
40	13.4	1.0	13.06	71.8	11.6	1.1	9.90	1.85
60	13.8	1.3	13.13	72.2	11.8	0.9	9.47	4.57
25 (Cooled)	14.3	1.3	13.08	71.9	11.7	0.7	9.19	9.72

The average fitted XRR thickness of four different graphene samples from two different sample batches at 25 °C was $t_g = 13.0 \pm 1.0$ Å (Table S3), slightly smaller than the AFM thickness of 13.9 ± 0.7 Å (Fig. 3d), which nonetheless is broadly consistent with the conclusion that the graphene layer was FLG with an average of 3–4 graphene monolayers. This is probably due to XRR measurements giving an average thickness over a much larger footprint (~10^6 μm^2), while AFM measures the local apparent thickness (with a footprint of ~1 μm^2) that is affected by the interaction between the tip and the surface. The total thickness of graphene and the contaminant layers from XRR fitting was ~25 Å, close to the thickness (27.1 ± 0.8 Å) obtained from the ellipsometry measurement on the same graphene samples.

The coverage of each layer can be calculated by comparing the fitted ρ with theoretical values, *i.e.* $\phi = \rho_{fitted}/\rho_{calculated}$. The fitted ρ values of each layer are shown in, the theoretical ρ of each material is listed in Table S2; the calculated SLD for graphene is $\rho_g = 1.820 \times 10^{-5}$ Å^{-2} at 14 keV. The graphene coverage at room temperature from XRR is $\phi_g = 76.3 \pm 7.0\%$, broadly consistent with the value ϕ_g ~$85.1 \pm 2.1\%$ estimated from AFM imaging, with the discrepancy again ascribable to the differences in the footprint size the two techniques probe. As such, the XRR ϕ_g value is an average over a much larger sample area, compared to the localised information from AFM imaging.

An interesting observation is that the graphene layer thickness t_g experienced a subtle expansion from 12.9 Å at 25 °C to 13.8 Å at 60 °C, and the roughness $R_{a,g}$ from 0.9 Å to 1.3 Å correspondingly. Meanwhile, the thickness of the contaminant layer remained largely constant at $t_c = 11.7$ Å, but its roughness $R_{a,c}$ decreased from 1.2 Å to 0.9 Å from 25 °C to 60 °C, suggesting a possible "curing" procedure upon heating, leading to a reduction of the roughness. The $R_{a,c}$ value continued to decrease to 0.7 Å, suggesting possible further relaxation. Furthermore, this change in the graphene layer thickness was irreversible; since after cooling to 25 °C, t_g further increased slightly to 14.3 Å. This observation might be explained by the out-of-plane motion of graphene, which may also be considered as a perpendicular thermal expansion or enhanced surface ripples. Unlike most of other materials, including SiO_2 and PMMA, graphene was demonstrated both theoretically and experimentally to have a negative in-plane thermal expansion coefficient (TEC) below ~500 K, as a consequence of decreasing phonon energies exhibited by 2D materials with smaller lattice parameters (rippled) upon heating, in contrast to increasing phonon energies in bulk materials [45–47]. In addition, the asymmetric bond length distribution of graphene caused by the delocalized p-cloud and the structural defects forces graphene to become non-planar to minimize free energy [48]. The rippling of graphene supported by Si/SiO_2 upon heating above 200 K was observed with SEM [49] and Raman spectroscopy [47]. When graphene attached to a SiO_2 substrate is heated, the graphene layer would experience an in-plane compressive stress because of its negative TEC, while SiO_2 would have experienced a tensile stress. Once the force applied on graphene exceeds the vdW attractive force between graphene and the substrate (normally at higher temperature), graphene might escape from the underling layer to enhance the amplitude of the ripples. This is also consistent with our observation that, after cooling back to room temperature, the graphene layer thickness detected by XRR further increased. This could be attributed to the tension on the graphene being smaller than the pining force, and the graphene stayed attached to the substrate, manifesting in enhanced rippling. We should acknowledge that our conclusions on the temperature dependence of the graphene sample thickness are tentative at this stage, and more measurements are needed to further verify these interesting and important observations.

4. Concluding remarks

The physical properties of graphene are intimately dependent on its thickness and surface structure. Understanding the surface structure of graphene is also important to its integration in composite materials and its bioanalytic applications. In this study, XRR was used to study the thickness of commercially sourced graphene prepared using the CVD method on Si/SiO_2 in air at different temperatures for the first time. Such graphene samples have been widely used in research and applications on monolayer graphene. Complementary techniques as AFM, XPS, and PEEM have been used to provide information on topography and chemical compositions of the graphene layer. Our XRR and AFM results show that the thickness of the graphene layer was ~13.0 ± 1.0 Å and 13.9 ± 0.7 Å, respectively, corresponding to 3–4 graphene monolayers. As such, the samples we characterized appeared to consist of 3–4 monolayers of graphene. This may suggest that other such commercial graphene samples are not of monolayer character. Given that XRR has not been previously widely used for studying the graphene structure, we hope to stimulate further investigations rather than regarding our conclusions as certainty and applicable to all commercial graphene samples. The XPS and PEEM results suggest the presence of PMMA residues from the transfer process of graphene fabrication. In addition, isolated islands of multilayer graphene were also present atop the FLG layer. We also observed a slight but detectable increase of 0.5–0.9 Å in the graphene layer thickness as it was heated from room temperature to 60 °C. This thermal expansion was irreversible, with the graphene thickness increasing a further 0.5 Å upon cooling back to room temperature. Such temperature dependent graphene thickness could be attributed to the out of plane rippling behaviour of graphene upon heating as previously reported. We should acknowledge that our conclusions on the temperature dependence of the graphene sample thickness are tentative at this stage, and more measurements are needed to further verify these interesting and important observations. These results on the FLG surface structure and chemistry are valuable to its potential bioanalytical applications where its interactions with biomolecules are an important consideration.

Acknowledgement

We acknowledge funding from the Engineering and Physical Science Research Council (EPSRC EP/H034862/1, and EP/L016648/1

through the *Bristol Centre for Functional Nanomaterials* (BCFN)), the Royal Society, Taiho Kogyo Tribology Research Foundation, the European Cooperation in Science and Technology (CMST COST) Action CM1101, the Marie Curie Initial Training Network (MC-ITN) "*Soft, Small, and Smart: Design, Assembly, and Dynamics of Novel Nanoparticles for Novel Industrial Applications (NanoS3)*" (FP7 Grant No. 290251), and the Consejo Nacional de Ciencia y Tecnologia (CONACyT) Postdoctoral Fellowship 291231. We also thank Procter & Gamble for financial support via the Bristol Final Year Industrial Project Scheme. Synchrotron X-ray access at EPSRC funded ESRF CRG XMas beamline and the support by the beamline staff is acknowledged. The authors acknowledge the Bristol NanoESCA Facility EPSRC Strategic Equipment Grant EP/M000605/1.

Appendix A. Supplementary data

Supplementary data related to this article can be found at https://doi.org/10.1016/j.carbon.2018.04.089.

References

[1] K.S. Novoselov, A.K. Geim, S.V. Morozov, D. Jiang, Y. Zhang, S.V. Dubonos, et al., Electric field effect in atomically thin carbon films, Science 306 (5696) (2004) 666–669.
[2] K.S. Novoselov, V.I. Fal'ko, L. Colombo, P.R. Gellert, M.G. Schwab, K. Kim, A roadmap for graphene, Nature 490 (7419) (2012) 192–200.
[3] A.K. Geim, Graphene: status and prospects, Science 324 (5934) (2009) 1530–1534.
[4] P.K. Ang, W. Chen, A.T.S. Wee, K.P. Loh, Solution-gated epitaxial graphene as pH sensor, J. Am. Chem. Soc. 130 (44) (2008) 14392. -+.
[5] P.K. Ang, M. Jaiswal, C. Lim, Y. Wang, J. Sankaran, A. Li, et al., A bioelectronic platform using a graphene-lipid bilayer interface, ACS Nano 4 (12) (2010) 7387–7394.
[6] D.C. Wang, Y.M. Zhang, Spectroscopic and scanning probe analysis on large-area epitaxial graphene grown under pressure of 4 mbar on 4H-SiC (0001) substratesl, Chin. Phys. B 23 (7) (2014) 6.
[7] R. Kadowaki, M. Kuriyama, T. Abukawa, K. Sagisaka, D. Fujita, PEEM and micro PES study of graphene growth on Ni(110) substrate, E-Journal of Surface Science and Nanotechnology 13 (2015) 347–351.
[8] W. Liu, H. Li, C. Xu, Y. Khatami, K. Banerjee, Synthesis of high-quality monolayer and bilayer graphene on copper using chemical vapor deposition, Carbon 49 (13) (2011) 4122–4130.
[9] X.S. Li, Y.W. Zhu, W.W. Cai, M. Borysiak, B.Y. Han, D. Chen, et al., Transfer of large-area graphene films for high-performance transparent conductive electrodes, Nano Lett. 9 (12) (2009) 4359–4363.
[10] S. Unarunotai, Y. Murata, C.E. Chialvo, H.S. Kim, S. MacLaren, N. Mason, et al., Transfer of graphene layers grown on SiC wafers to other substrates and their integration into field effect transistors, Appl. Phys. Lett. (20) (2009) 95.
[11] J.W. Suk, A. Kitt, C.W. Magnuson, Y.F. Hao, S. Ahmed, J.H. An, et al., Transfer of CVD-grown monolayer graphene onto arbitrary substrates, ACS Nano 5 (9) (2011) 6916–6924.
[12] J.D. Caldwell, T.J. Anderson, J.C. Culbertson, G.G. Jernigan, K.D. Hobart, F.J. Kub, et al., Technique for the dry transfer of epitaxial graphene onto arbitrary substrates, ACS Nano 4 (2) (2010) 1108–1114.
[13] C. Mattevi, H. Kim, M. Chhowalla, A review of chemical vapour deposition of graphene on copper, J. Mater. Chem. 21 (10) (2011) 3324–3334.
[14] M.S. Xu, D. Fujita, J.H. Gao, N. Hanagata, Auger electron spectroscopy: a rational method for determining thickness of graphene films, ACS Nano 4 (5) (2010) 2937–2945.
[15] W.Y. Jang, Z. Chen, W.Z. Bao, C.N. Lau, C. Dames, Thickness-dependent thermal conductivity of encased graphene and ultrathin graphite, Nano Lett. 10 (10) (2010) 3909–3913.
[16] G.M. Rutter, J.N. Crain, N.P. Guisinger, T. Li, P.N. First, J.A. Stroscio, Scattering and interference in epitaxial graphene, Science 317 (5835) (2007) 219–222.
[17] Z.H. Aitken, R. Huang, Effects of mismatch strain and substrate surface corrugation on morphology of supported monolayer graphene, J. Appl. Phys. 107 (12) (2010) 10.
[18] D.S. Geng, S.L. Yang, Y. Zhang, J.L. Yang, J. Liu, R.Y. Li, et al., Nitrogen doping effects on the structure of graphene, Appl. Surf. Sci. 257 (21) (2011) 9193–9198.
[19] J.Q. Xu, P. Kruger, C.R. Natoli, K. Hayakawa, Z.Y. Wu, K. Hatada, X-ray absorption spectra of graphene and graphene oxide by full-potential multiple scattering calculations with self-consistent charge density, Phys. Rev. B 92 (12) (2015).
[20] R. Frost, G.E. Jonsson, D. Chakarov, S. Svedhem, B. Kasemo, Graphene oxide and lipid membranes: interactions and nanocomposite structures, Nano Lett. 12 (7) (2012) 3356–3362.
[21] W.H. Briscoe, M. Chen, I.E. Dunlop, J. Klein, J. Penfold, R.M.J. Jacobs, Applying grazing incidence X-ray reflectometry (XRR) to characterising nanofilms on mica, J. Colloid Interface Sci. 306 (2) (2007) 459–463.
[22] R.P. Giri, A. Chakrabarti, M.K. Mukhopadhyay, Cholesterol-induced structural changes in saturated phospholipid model membranes revealed through X-ray scattering technique, J. Phys. Chem. B 121 (16) (2017) 4081–4090.
[23] F. Speranza, G.A. Pilkington, T.G. Dane, P.T. Cresswell, P.X. Li, R.M.J. Jacobs, et al., Quiescent bilayers at the mica-water interface, Soft Matter 9 (29) (2013) 7028–7041.
[24] B. Sironi, T. Snow, C. Redeker, A. Slastanova, O. Bikondoa, T. Arnold, et al., Structure of lipid multilayers via drop casting of aqueous liposome dispersions, Soft Matter 12 (17) (2016) 3877–3887.
[25] S.J. Jeong, Y. Gu, J. Heo, J. Yang, C.S. Lee, M.H. Lee, et al., Thickness scaling of atomic-layer-deposited HfO2 films and their application to wafer-scale graphene tunnelling transistors, Sci. Rep. 6 (2016).
[26] M. Kalbac, V. Vales, J. Vejpravova, The effect of a thin gold layer on graphene: a Raman spectroscopy study, RSC Adv. 4 (105) (2014) 60929–60935.
[27] J.D. Emery, Q.H. Wang, M. Zarrouati, P. Fenter, M.C. Hersam, M.J. Bedzyk, Structural analysis of PTCDA monolayers on epitaxial graphene with ultra-high vacuum scanning tunneling microscopy and high-resolution X-ray reflectivity, Surf. Sci. 605 (17–18) (2011) 1685–1693.
[28] M. Conrad, J. Rault, Y. Utsumi, Y. Garreau, A. Vlad, A. Coati, et al., Structure and evolution of semiconducting buffer graphene grown on SiC(0001), Phys. Rev. B 96 (19) (2017).
[29] J.D. Emery, V.D. Wheeler, J.E. Johns, M.E. McBriarty, B. Detlefs, M.C. Hersam, et al., Structural consequences of hydrogen intercalation of epitaxial graphene on SiC(0001) (vol. 105, 161602, 2014), Appl. Phys. Lett. 107 (18) (2015).
[30] W.Y. Li, K. Goto, R. Shimizu, PEEM is a suitable tool for absolute work function measurements, Surf. Interface Anal. 37 (2) (2005) 244–247.
[31] W.H. Briscoe, F. Speranza, P.X. Li, O. Konovalov, L. Bouchenoire, J. van Stam, et al., Synchrotron XRR study of soft nanofilms at the mica-water interface, Soft Matter 8 (18) (2012) 5055–5068.
[32] A. Nelson, Co-refinement of multiple-contrast neutron/X-ray reflectivity data using MOTOFIT, J. Appl. Crystallogr. 39 (2006) 273–276.
[33] S. Stankovich, D.A. Dikin, R.D. Piner, K.A. Kohlhaas, A. Kleinhammes, Y. Jia, et al., Synthesis of graphene-based nanosheets via chemical reduction of exfoliated graphite oxide, Carbon 45 (7) (2007) 1558–1565.
[34] B. Lesiak, L. Stobinski, A. Malolepszy, M. Mazurkiewicz, L. Kover, J. Toth, Preparation of graphene oxide and characterisation using electron spectroscopy, J. Electron. Spectrosc. Relat. Phenom. 193 (2014) 92–99.
[35] L. Stobinski, B. Lesiak, A. Malolepszy, M. Mazurkiewicz, B. Mierzwa, J. Zemek, et al., Graphene oxide and reduced graphene oxide studied by the XRD, TEM and electron spectroscopy methods, J. Electron. Spectrosc. Relat. Phenom. 195 (2014) 145–154.
[36] Y.C. Lin, C.C. Lu, C.H. Yeh, C.H. Jin, K. Suenaga, P.W. Chiu, Graphene annealing: how clean can it Be? Nano Lett. 12 (1) (2012) 414–419.
[37] R.S. Yan, Q. Zhang, W. Li, I. Calizo, T. Shen, C.A. Richter, et al., Determination of graphene work function and graphene-insulator-semiconductor band alignment by internal photoemission spectroscopy, Appl. Phys. Lett. 101 (2) (2012).
[38] C.S.A. Fang, C.E. Maloney, The effect of substrate work function on work function reduction of Re/W alloy-coated impregnated cathodes, Appl. Phys. Mater. Sci. Process 50 (6) (1990) 603–607.
[39] M.T. Greiner, M.G. Helander, W.M. Tang, Z.B. Wang, J. Qiu, Z.H. Lu, Universal energy-level alignment of molecules on metal oxides, Nat. Mater. 11 (1) (2012) 76–81.
[40] H. Hibino, H. Kageshima, M. Kotsugi, F. Maeda, F.Z. Guo, Y. Watanabe, Dependence of electronic properties of epitaxial few-layer graphene on the number of layers investigated by photoelectron emission microscopy, Phys. Rev. B (12) (2009) 79.
[41] S.S. Datta, D.R. Strachan, E.J. Mele, A.T.C. Johnson, Surface potentials and layer charge distributions in few-layer graphene films, Nano Lett. 9 (1) (2009) 7–11.
[42] P. Nemes-Incze, Z. Osvath, K. Kamaras, L.P. Biro, Anomalies in thickness measurements of graphene and few layer graphite crystals by tapping mode atomic force microscopy, Carbon 46 (11) (2008) 1435–1442.
[43] A.N. Sidorov, M.M. Yazdanpanah, R. Jalilian, P.J. Ouseph, R.W. Cohn, G.U. Sumanasekera, Electrostatic deposition of graphene, Nanotechnology 18 (13) (2007).
[44] Z.H. Chen, Y.M. Lin, M.J. Rooks, P. Avouris, Graphene nano-ribbon electronics, Phys. E Low-dimens. Syst. Nanostruct. 40 (2) (2007) 228–232.
[45] P.K. Schelling, R. Keblinski, Thermal expansion of carbon structures, Phys. Rev. B (3) (2003) 68.
[46] M.Z. Islam, M. Mahboob, R.L. Lowe, Characterization of the thermal expansion properties of graphene using molecular dynamics simulations (vol. 46, 435302, 2013), J. Phys. Appl. Phys. 47 (40) (2014).
[47] D. Yoon, Y.W. Son, H. Cheong, Negative thermal expansion coefficient of graphene measured by Raman spectroscopy, Nano Lett. 11 (8) (2011) 3227–3231.
[48] S.K. Deng, V. Berry, Wrinkled, rippled and crumpled graphene: an overview of formation mechanism, electronic properties, and applications, Mater. Today 19 (4) (2016) 197–212.
[49] W.Z. Bao, F. Miao, Z. Chen, H. Zhang, W.Y. Jang, C. Dames, et al., Controlled ripple texturing of suspended graphene and ultrathin graphite membranes, Nat. Nanotechnol. 4 (9) (2009) 562–566.